Hindawi
Advances in Materials Science and Engineering
Volume 2019, Article ID 2960435, 14 pages
https://doi.org/10.1155/2019/2960435

Research Article

Structural Design of Mechanical Property for Biodegradable Polymeric Stent

Yunbo Wei,[1] **Minjie Wang**,[1] **Danyang Zhao**,[1] **Hongxia Li**,[1] **and Yifei Jin**[2]

[1]*Department of Mechanical Engineering, Dalian University of Technology, Dalian 116023, China*
[2]*Department of Mechanical Engineering, University of Nevada Reno, Reno 89557, NV, USA*

Correspondence should be addressed to Minjie Wang; mjwang@dlut.edu.cn

Received 4 July 2019; Revised 21 September 2019; Accepted 25 October 2019; Published 10 December 2019

Academic Editor: Fabrizio Sarasini

How to improve stent mechanical properties is a key issue for designing biodegradable polymeric stents (BPSs). In this study, a new design method of BPS was proposed based on the force analysis of supporting rings and bridges during stent implantation, and a novel BPS called open *C*-shaped stent (OCS) with superior comprehensive mechanical properties was developed accordingly. The key mechanical properties including radial force, radial recoil, and axial foreshortening of the OCS have been comprehensively studied and compared with those of the Abbott BVS using finite element analysis (FEA). In addition, the effects of the stent geometries on these mechanical properties have also been discussed in detail. Besides, *in vitro* mechanical tests including stent expansion and planar compression experiments have been performed to verify the simulation results. Based on the FEA results, it is found that the radial force and radial recoil of the designed OCS are 30% higher and 24% lower than those of the BVS, respectively. Meanwhile, the OCS is not shortened during expansion. Radial force and radial recoil are mainly dependent on the supporting ring structure, and the utilization of designed unequal-height supporting ring (UHSR) can effectively improve these two properties. Axial foreshortening is mainly determined by the bridge geometry as well as the connecting position of the bridge with the adjacent supporting rings. It is feasible to improve the axial foreshortening by using the bridges with a curved structure and locating the connecting position in the middle of the straight section of the supporting elements. The rationality of the proposed OCS and the effectiveness of the finite element method have been verified by *in vitro* experiments.

1. Introduction

Biodegradable vascular stents are hailed as the fourth revolution in coronary intervention [1]. They provide temporary support to diseased blood vessels and disappears gradually, which overcome the core complications induced by the permanent retention of traditional metallic stents including vasomotor dysfunction, late in-stent restenosis and revascularization of advanced target lesions [2–4]. Based on the superior biocompatibility, biodegradability, and processability of biodegradable polymers, BPS has become a subject of current interest [5, 6]. However, due to the relatively weak mechanical properties of polymers comparing with metals, the resulted polymeric stents usually have worse mechanical performance, in particular the poor radial force and radial recoil [7–9]. As a result, how to improve the mechanical properties of BPSs has become the main challenge.

Apart from the modification of build materials [10, 11], two strategies have been developed to improve the mechanical properties of BPSs: (1) increasing strut thickness [12–14] and (2) changing stent structure. For the former one, the increase of strut thickness can effectively improve the radial force, while it also results in the increase of the entire profile, which leads to the increasing risk of in-stent restenosis and limits the treatments for heavily curved or highly calcified diseased vessels [15]. For the latter one, undoubtedly, the stent structure has a dramatic effect on stent mechanical properties including but not limited to radial force, radial recoil, flexibility, and axial foreshortening

[16]. As a result, this strategy has widely been investigated to design BPSs with excellent mechanical performance. Some of the representative results are summarized as follows. Schiavone et al. [17] investigated the radial recoil of four commercial stents with various structures using FEA, and they found that stents with distinct structures showed a considerable difference in radial recoil. Wu et al. [18] and Hsiao et al. [19] investigated the effects of supporting rings with a sinusoidal structure on the radial force of the stents, and they found that the strut width had the most considerable effects among all the structural parameters. However, their studies only focused on the structural parameters, and effects of structural patterns on the mechanical properties were ignored. Shen et al. [20], Bobel et al. [21], and Bae et al. [22] proposed several stents with different bridge geometries and studied the effects of the bridge geometry on the flexibility of the stents, whereas the effects of the bridge geometry on the other mechanical properties including radial recoil and axial foreshortening were not discussed. Feng et al. [23] proposed a new type of BPS based on the slide and lock mechanism to maximize the radial force. However, due to the complexity of the slide-lock stents, localized mechanical wear can happen during sliding, which increases the risk of artery wall damage [24]. From these reported results, it can be seen that although many BPSs with different structures have been proposed, these structures are only based on the improvement of one specific mechanical property. There are few studies on the structural design considering the comprehensive mechanical properties of a BPS and the influence of stent structures on these mechanical properties. In addition, the aforementioned studies only used the finite element methods to analyze stent mechanical properties, lacking the necessary experimental verification.

In this study, a novel BPS is proposed based on the force analysis of the supporting rings and bridges during stent implantation. Using the finite element method, the mechanical properties of the proposed stent including radial force, radial recoil, and axial foreshortening are investigated and compared with those of the BVS. In addition, the effects of the stent structures on these mechanical properties are systematically studied. Finally, *in vitro* expansion and planar compression experiments are performed to further evaluate the mechanical properties of both the proposed stent and the BVS.

2. Structural Design of BPS

BPS is generally composed of supporting rings and bridges. Supporting rings are the core elements to provide scaffolding to restore and maintain the patency of diseased vessels, and bridges function as connections of adjacent supporting rings. A typical BPS is the Abbott BVS [25], which has acquired FDA approval and is constructed by sinusoid-shaped supporting rings with equal-height wave amplitude (EHSR) and straight rod-shaped bridges as shown in Figure 1. The basic unit of a supporting ring is referred to as the supporting element. The connection pattern between supporting rings and bridges is open cell style, i.e., there are more than one peaks and/or troughs in a mesh encircled by two adjacent supporting rings and two adjacent bridges. Due to the simple geometries, the BVS is easy to be fabricated and has excellent flexibility. However, the poor radial force makes the BVS have a wall thickness larger than that of metallic stents in order to achieve the desired radial force [24].

In this study, in order to develop a BPS with superior comprehensive mechanical properties, including radial force, radial recoil, and axial foreshortening, force analysis of supporting rings and bridges during stent implantation is first carried out.

2.1. Supporting Ring Design. The supporting ring plays a major role to maintain the stent shape in narrowed blood vessels. After stent implantation, the external surface of the stent is subjected to pressure p exerted by the blood vessel wall, as shown in Figure 2(a). Since the supporting ring is composed of several repetitive supporting elements, half of one supporting element of the supporting ring is taken as the research object for analysis. Figures 2(b) and 2(c) are the front and axial views of the semisupporting element, respectively. r is the average radius of the stent, β_0 is approximately half of the strut angle of the supporting element, α_0 is the circumferential angle of the semisupporting element, w and t are the strut width and thickness, respectively, and h is the height of the supporting element. Cartesian coordinate systems xyz and $x'y'z'$ are defined on both ends of the semisupporting element, and the origins of the two coordinate systems are located at the centroids of the two ends. The x-axis and the x'-axis are perpendicular to the two end faces, respectively, the y-axis and y'-axis are parallel to the axis of the supporting ring, and the z-axis and z'-axis are along the radial direction of the supporting ring. Under the action of external pressure p, the two ends of the semisupporting element are subjected to the forces F_x and $F_{x'}$ and the bending moments M_z and $M_{z'}$, as shown in Figure 2(b). According to the symmetry and equilibrium equations, the forces and bending moments can be expressed as [26]

$$F_x = F_{x'} = \frac{p \cdot w \cdot r}{\sin \beta_0}, \tag{1}$$

$$M_z = M_{z'} = \frac{p \cdot w \cdot r \cdot h \cdot \cos^2(\alpha_0/2)}{2 \sin \beta_0}. \tag{2}$$

It can be seen from equations (1) and (2) that both F_x and M_z, the two main factors causing stent radial deformation or even collapse, decrease with the increase of β_0. As a result, the increase of the strut angle after stent expansion is helpful to improve the radial supporting capability. However, if strut angles of all supporting elements increase, the expansion range of stent will be reduced. Accordingly, in order to obtain a stent with higher radial supporting capability without sacrificing its expansion range, a supporting ring composed of several alternatively distributed supporting elements with unequal-height wave amplitude was proposed, referred to as unequal-height supporting ring

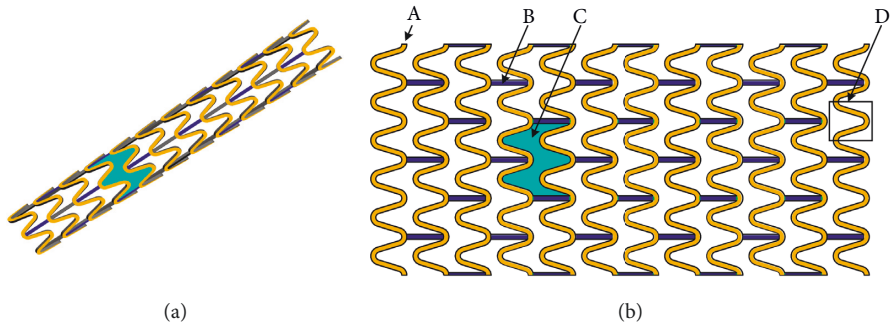

Figure 1: Schematic of the structure of a typical BPS: (a) three-dimensional (3D) model; (b) two-dimensional (2D) model. (A) supporting ring; (B) straight rod-shaped bridge; (C) open cell; (D) supporting element.

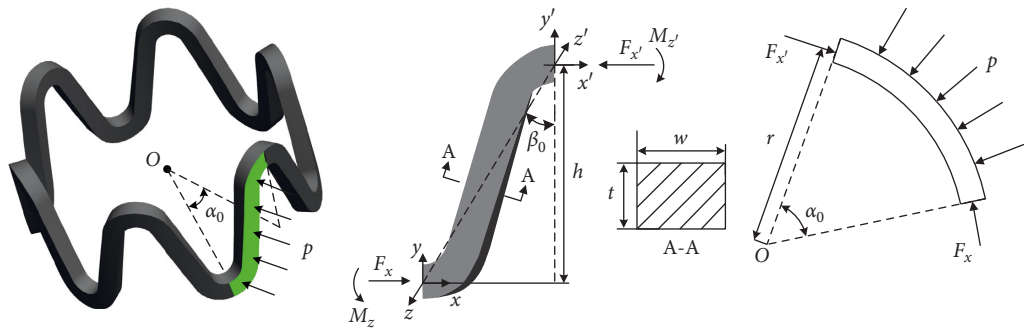

Figure 2: Diagram of supporting ring under external pressure: (a) the supporting ring; (b) the front view of the semisupporting element; (c) the axial view of the semisupporting element.

(UHSR). The axial distance between the peak (or valley) of the small supporting element and the peak (or valley) of adjacent big supporting element is δ, as shown in Figure 3. The main feature of the UHSR is that with the same circumferential displacement increment, the small supporting element has a larger final strut angle comparing with the big supporting element. The geometric relationships are analyzed as follows.

The geometrical relationships of the simplified supporting elements are` illustrated in Figure 4. The big element and small supporting element are simplified to isosceles triangles ΔABC and ΔGBC, respectively. The strut angles corresponding to these two triangles are β_1 and β_2, respectively. When the length of the bottom line increases by Δl, two isosceles triangles can be converted into ΔABE and ΔGBF, respectively. Correspondingly, the increments of the two strut angles can be expressed as $\Delta\beta_1$ and $\Delta\beta_2$, respectively. As a result, the following equations can be obtained:

$$\cos(\Delta\beta_1) = \frac{2l_1^2 - d_2^2}{2l_1^2},$$
$$\cos(\Delta\beta_2) = \frac{2l_2^2 - d_1^2}{2l_2^2}. \tag{3}$$

Through further derivation, the following equation can be achieved:

$$\cos(\Delta\beta_1) - \cos(\Delta\beta_2) = \frac{1}{2l_1^2 \cdot l_2^2} \times \left[\left((l+\Delta l)^2 + l^2 - 2(l+\Delta l) \cdot l \cdot \cos\gamma_2 \right) \cdot l_1^2 - \left((l+\Delta l)^2 + l^2 - 2 \cdot (l+\Delta l) \cdot l \cdot \cos\gamma_1 \right) \cdot l_2^2 \right]. \tag{4}$$

Given $l_1 > l_2$,

$$\cos(\Delta\beta_1) - \cos(\Delta\beta_2) > \frac{2(l+\Delta l) \cdot l \cdot (\cos\gamma_1 - \cos\gamma_2)}{2l_1^2}. \tag{5}$$

As seen in Figure 4, it is found that γ_1 is smaller than γ_2, and both these angles are sharp angles. Meanwhile, considering the practical application of stents, the increments of both β_1 and β_2 must be less than 90°. Thus, based on equation (5), the relationship $\cos(\Delta\beta_1) - \cos(\Delta\beta_2) > 0$ can be deduced, indicating that $\Delta\beta_1 < \Delta\beta_2$. As a result, the increment of the strut angle of the small supporting element is larger than that of the big supporting element under the same circumferential displacement increment. Furthermore, since the initial strut angle β_2 is larger than β_1, the final strut angle at the inflated state of the small supporting element is larger than that of the big supporting element. Therefore, a stent

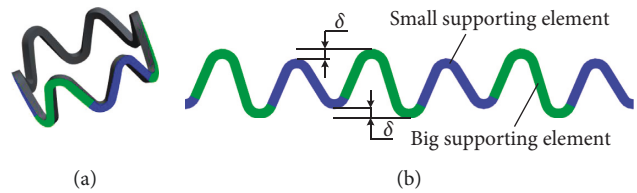

Figure 3: Schematic of the UHSR: (a) 3D UHSR; (b) 2D UHSR.

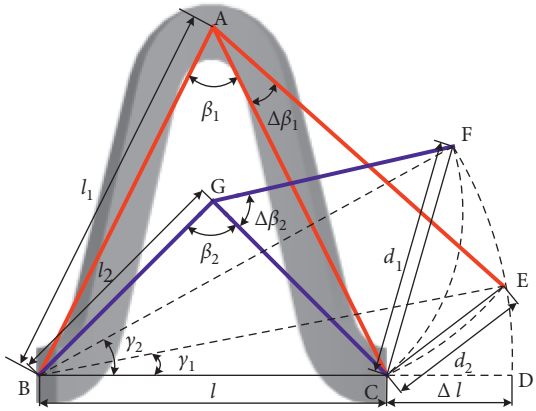

Figure 4: Geometrical relationships of the simplified supporting elements.

using UHSR has better radial supporting capability under compressive load comparing with the stent using EHSR.

2.2. Bridge Design. Although mainly playing a role in connecting adjacent supporting rings, bridges also have a potential impact on axial foreshortening. During inflation, pressure P exerted by balloon is applied to the internal surface of the stent, as shown in Figures 5(a) and 5(b). Thus, the cross section of a supporting element is subjected to circumferential tension F_t, which leads the expansion of stents. The relationship between F_t and P can be described as

$$F_t = \frac{P \cdot S}{2 \sin(\alpha/2)}, \tag{6}$$

where α is the radian of the supporting element along the circumferential direction and S is the internal surface area of the supporting element in the range of α. In order to obtain the relationship between pressure P and axial tension force acting on the bridge, the supporting element is simplified to a plane isosceles triangle, as shown in Figure 5(c). From Figures 5(b) and 5(c), we can easily get $F_t' = F_t \cos(\alpha/2)$, where F_t' is the circumferential tension force in the simplified model. F_t' can be further decomposed into two component forces: F_1 and F_2. As seen in Figure 5(c), F_1 is the primary component force leading to the stent expansion, while F_2 mainly results in the axial movement as well as the height decrease of the supporting element, which contributes to the stent shortening behavior during expansion. It is noted that during the deformation of the supporting element, the bridge is subjected to an axial tension T, which can be expressed as

$$T = \frac{P \cdot S \cdot \sin\beta \cot(\alpha/2)}{2}, \tag{7}$$

where β is the strut angle. If the bridge can elongate under the action of T, the elongation may compensate the shortening of the supporting element, which means that the axial foreshortening of the stent will decrease. Unfortunately, currently used bridges in BPSs such as the commercial stent BVS are generally straight rod-shaped and cannot be elongated under the axial tension force. As a result, bridge design is helpful to overcome the challenge of stent shortening during implantation. As is known to everyone, a curved structure is easier to deform comparing with a straight structure under tension force. Thus, a bridge with curved structure is proposed in this study. In addition, since laser cutting is the main method to fabricate BPSs, which usually results in the severe heat-affected zone, the curvature of the bridge cannot be too large.

2.3. Stent Design. Comparing with traditional metallic stents, BPSs are made from softer polymer composites, which results in the excellent flexibility of the polymeric stents. Therefore, in the design of BPSs, three key mechanical properties including radial force, radial recoil, and axial foreshortening are used as the criteria to evaluate the rationality of the design. Based on the knowledge from the supporting ring and bridge design, an open C-shaped stent (OCS) is developed as is shown in Figure 6.

The main features of the OCS are listed as follows: all supporting rings except those at both ends employ the structure of UHSR to achieve better radial force. The two adjacent UHSRs are arranged with opposite phases (with a phase difference of 90°), which leads to the larger space for bridge arrangement and avoids interference of the adjacent UHSRs during stent bending. Except those at both ends, all bridges are designed as a C-shaped structure to improve the axial foreshortening. Connecting positions of C-shaped bridges are located in the middle of the straight section of the supporting element so that the bridges have a larger curvature radius and can be easily fabricated. The pattern of connection between supporting rings and bridges is designed as an open cell style, which can improve the flexibility. In addition, the orientation of two adjacent rows of C-shaped bridges is reversed to prevent stent rotation during expansion.

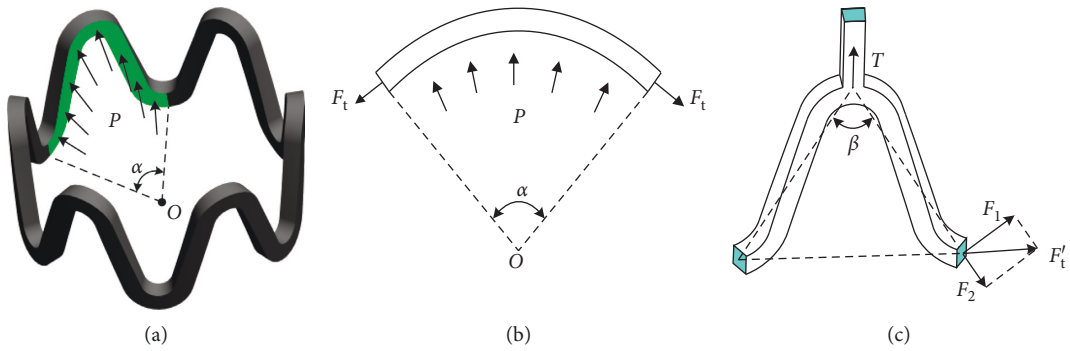

Figure 5: Diagram of the supporting ring under the balloon pressure: (a) 3D supporting ring; (b) the axial view of the supporting element; (c) the front view of the supporting element.

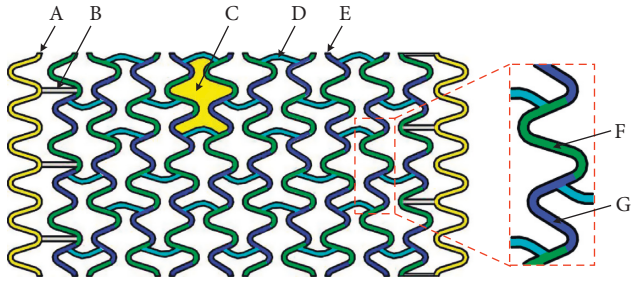

Figure 6: 2D schematic of the OCS. (A) equal-height supporting ring; (B) straight rod-shaped bridge; (C) open cell (D) c-shaped bridge; (E) unequal-height supporting ring; (F) small supporting element; (G) big supporting element.

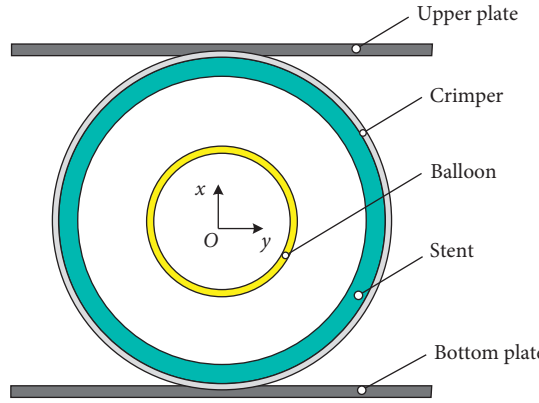

Figure 7: Schematic of stent crimping, expansion, and planar compression simulation.

3. Finite Element Analysis

FEA has widely been used as a powerful tool to design and evaluate stent mechanical properties. In this study, a comparative analysis on radial force, radial recoil, and axial foreshortening of the OCS and BVS is performed using FEA. The simulations were conducted using finite element package (ANSYS Inc., Canonsburg, PA, USA). For reliable comparison, the OCS and BVS have the same original outer diameter of 2.40 mm, strut width of 0.14 mm, and strut thickness of 0.14 mm. The lengths of these two stents are 15.50 mm and 16.10 mm, respectively. The number of supporting elements along the circumferential direction of the supporting ring is identical for the both stents. Similarly, the height of the big supporting elements of the OCS is the same as that of the supporting elements of the BVS.

3.1. Finite Element Models. Stent crimping and expansion were first simulated to obtain the radial recoil and axial foreshortening of the OCS and BVS. After that, planar compression was simulated to evaluate the radial force. Figure 7 shows the schematic of the stent expansion and planar compression processes, and the main components include polymeric stent, crimper, balloon, and upper and bottom plates. The OCS and BVS models were meshed using 3D 8-node structural solid elements. Mesh sensitivity analysis was conducted on von Mises stress, von Mises total mechanical strain, and radial displacement with various element sizes starting from 3×3 per strut cross section to 6×6, as shown in Table 1. Mesh sensitivity analysis results showed that the above three indicators became stable when the mesh size was greater than 3×3. As a result, 4×4 was selected as the final element size for both the OCS and BVS. The total element numbers of the OCS and BVS were 101376 and 105504, respectively. The crimper, balloon, and upper and bottom plates were meshed using 4-node shell element, and the total element numbers were 60000, 24800, 28000, and 28000, respectively. The 3D finite element model of stent crimping, expansion, and planar compression processes is shown in Figure 8.

3.2. Material Properties. Polylactic acid (Ingeo 4032D, NatureWorks LLC, USA) was chosen as the stent material. The stress-strain curve was obtained by performing uniaxial tensile tests on fabricated dog-bone specimens, as shown in Figure 9. Young's modulus was calculated as 3546 MPa, the yield strength was calculated as 51.5 MPa, Poisson's ratio was 0.3, the plastic property data were provided based on the experimental stress-strain curve, and the material was assumed to be homogeneous and isotropic. The upper and bottom plates were assumed to be rigid planes. The crimper and balloon were made of nonlinear superelastic rubber material, which were

Table 1: Performed mesh sensitivity analysis.

Element size	3×3	4×4	5×5	6×6
von Mises stress (MPa)	59.2	61.1	60.7	58.9
von Mises total mechanical strain	0.14	0.15	0.15	0.15
Radial displacement (mm)	0.33	0.33	0.33	0.33

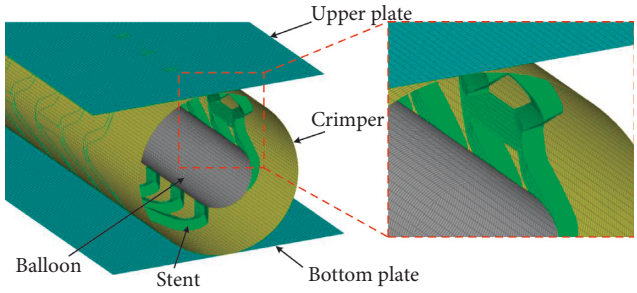

Figure 8: 3D finite element model of stent crimping, expansion, and planar compression processes.

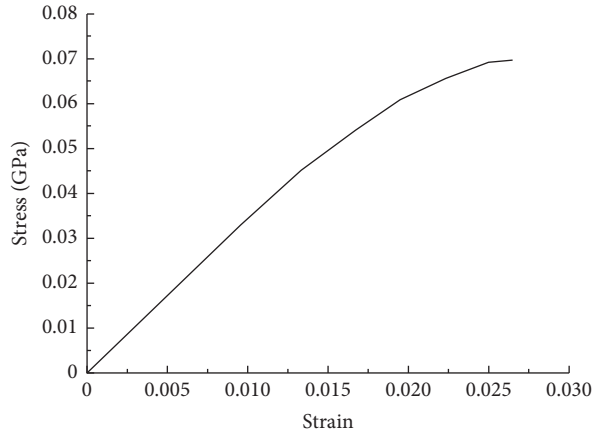

Figure 9: Stress-strain curve of the polylactic acid.

typically described by the Mooney–Rivlin constitutive model [27]. The Mooney–Rivlin constitutive model can be expressed as

$$W = \sum_{i=0,j=0}^{N} C_{ij} (I_1 - 3)^i (I_2 - 3)^j, \quad (8)$$

$$I_1 = \lambda_1^2 + \lambda_2^2 + \lambda_3^2, \quad (9)$$

$$I_2 = \lambda_1^2\lambda_2^2 + \lambda_2^2\lambda_3^2 + \lambda_1^2\lambda_3^2, \quad (10)$$

where W is the strain energy density function, C_{ij} is the parameter of the Mooney–Rivlin model, I_1 and I_2 are the first and second invariants of the left Cauchy–Green deformation tensor, respectively, and λ_1, λ_2, and λ_3 are the principal elongation ratio.

In this study, two-parameter Mooney–Rivlin model was assumed for the crimper and balloon, which was $N = 1$ in equation (8), and then the two-parameter Mooney–Rivlin constitutive model can be expressed as

$$W = C_{10}(I_1 - 3) + C_{01}(I_2 - 3), \quad (11)$$

where C_{10} and C_{01} can be obtained by fitting to experimental material properties. In this study, $C_{10} = 1.0688$ MPa and $C_{01} = 0.771018$ MPa [28].

3.3. Boundary Conditions. Since the comparative analysis was carried out in the identical conditions, the balloon was inflated using radial displacement load instead of pressure load to reduce the amount of calculation which has been proved not to affect the calculation results [29, 30]. In order to simulate the stent crimping, expansion, and planar compression, five loading steps were needed as follows:

(1) Stent crimping step, in which radial displacement was applied to crimper to crimp the stent to outer diameter of 1.35 mm. Surface to surface contacts between all the possible interaction surfaces were considered. Upper and bottom plates can move freely only in the x-direction.

(2) Stent recoil step, in which the displacement load applied to crimper was removed to allow the free elastic recoil of the crimped stent.

(3) Balloon inflation step: radial displacement was applied to the inner surface of the balloon to expand the stent to an outer diameter of 3.00 mm. The contact between crimper and outer surface of the stent were deactivated.

(4) Balloon deflation step: the radial displacement applied to the balloon was removed to allow the free elastic recoil of the expanded stent.

(5) Planar compression step: a linearly increasing pressure was imposed to the upper plate to compress the stent. Except for the contacts between plates and outer surface of the stent, all the other contacts were deactivated. All degrees of freedom of the bottom plate were constrained.

3.4. Finite Element Analysis Results. Deformations of the OCS and BVS at different steps are shown in Figure 10. It can be seen that the OCS and BVS were crimped uniformly to an outer diameter of 1.35 mm. Both in crimping and expanding process, there was no circumferential rotation and strut fracture. During balloon deflation, the stents experienced radial contraction, and diameters of the stents decreased. Finally, the stents were flattened with the increase of compressive load. The outer diameters and lengths of OCS and BVS at different steps are shown in Table 2.

Figure 11 shows the von Mises stress distributions for the OCS and BVS at different steps. It can be seen that the maximum stresses of the OCS at stent crimping and balloon inflation steps mainly occurred at the corners of the supporting rings and bridges (red area in Figure 11), and the value is 51.9 MPa. While for the BVS, maximum stresses occurred only at the corners of the supporting rings, which is consistent with that obtained by Qiu et al. [31], the value

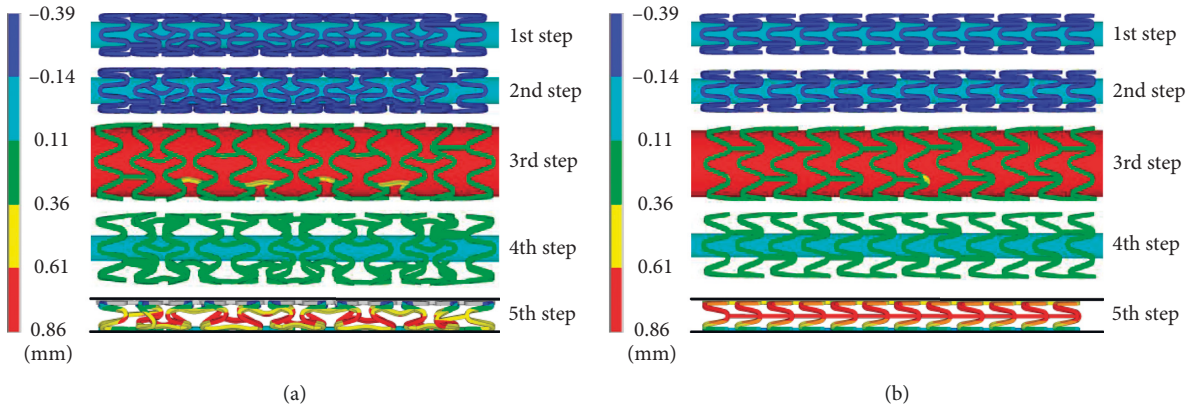

Figure 10: Deformations of the (a) OCS and (b) BVS at different steps during FEA.

Table 2: Outer diameters and lengths of the OCS and BVS at different steps during FEA.

Stent type	1st step		2nd step		3rd step		4th step	
	D_{crimp} (mm)	L_{crimp} (mm)	D_{recoil} (mm)	L_{recoil} (mm)	$D_{inflated}$ (mm)	$L_{inflated}$ (mm)	$D_{deflated}$ (mm)	$L_{deflated}$ (mm)
OCS	1.35	15.26	1.43	15.30	3.00	16.05	2.71	15.72
BVS	1.35	16.24	1.48	16.21	3.00	15.58	2.62	16.01

D_{crimp}: outer diameter of the crimped stent; L_{crimp}: length of the crimped stent; D_{recoil}: outer diameter of the stent at the stent recoil step; L_{recoil}: length of the stent at the stent recoil step; $D_{inflated}$: outer diameter of the stent at the inflated step; $L_{inflated}$: length of the stent at the inflated step; $D_{deflated}$: outer diameter of the stent at the deflated step; $L_{deflated}$: length of the stent at the deflated step.

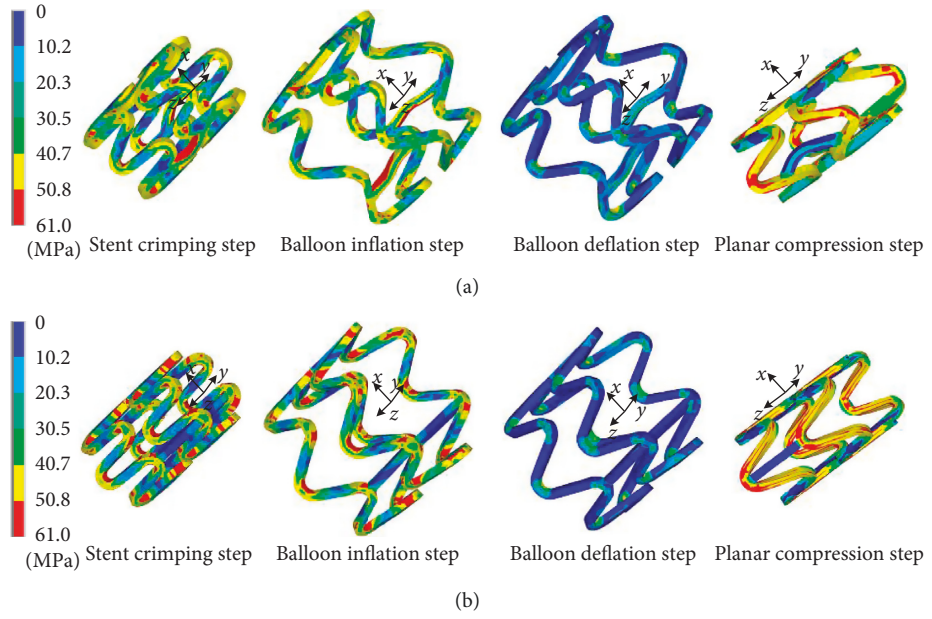

Figure 11: The von Mises stress distributions for the (a) OCS and (b) BVS at different steps.

was 51.3 MPa, and the stresses of the bridges of the BVS were almost zero. The maximum stress of the OCS was slightly greater than that of the BVS, which can be attributed to the more plastic deformation experienced by the supporting elements and bridges of the OCS. After balloon deflation, the maximum stresses of both these stents were concentrated in the area of the corners of the supporting rings, and the stresses decreased due to stent elastic contraction. In the planar compression process, the maximum stresses occurred at the corners of both sides of the supporting rings in the y-axis direction, and with the increase of the compressive load, the maximum stresses increased. It is worth noting that the stress of BVS bridges was still at a low level throughout the simulation, which means that there was almost no deformation of the BVS bridge.

3.4.1. Radial Recoil. Radial recoil refers to the diameter change of a stent before and after expansion, which is usually expressed as

$$\text{redial recoil} = \left(1 - \frac{D_{\text{deflated}}}{D_{\text{inflated}}}\right) \times 100\%. \quad (12)$$

According to the simulation results of stent expansion, the radial recoils of the OCS and BVS were calculated as 9.7% and 12.7%, respectively, indicating that the radial recoil of the OCS was reduced by approximately 24% comparing with that of the BVS, which can be explained by the utilization of the UHSRs in the OCS. It is noted that the stent recovery after balloon deflation is mainly caused by the elastic deformation of the stents at the inflated state. Thus, for the OCS, the small supporting element of the UHSR experiences a larger strut angle increment during balloon inflation, as discussed in Section 2.1, which indicates that larger plastic deformation zones are generated and the elastic deformation within the stent decreases. As a result, the radial recoil of the OCS was lower than that of the BVS. Another important factor contributing to the reduction of the radial recoil of the OCS is that the UHSR has better resistance against the elastic contraction. Figure 12 shows the force analysis of the supporting element under the action of elastic recoiling force. As is seen from Figure 12, the elastic recoiling force F_e exerted by the supporting element itself can be decomposed into a circumferential force F_{e1} and an axial force F_{e2}. F_{e1} is the primary component force leading to the reduction of stent diameter, which can be described as

$$F_{e1} = F_e \cos\theta. \quad (13)$$

From equation (13), it is observed that F_{e1} decreases with the increase of θ, which is about half of the strut angle β. Therefore, under the same elastic recoiling force F_e, the supporting element with the larger strut angle at the inflated state will undergo a lower circumferential force F_{e1}. Furthermore, based on the discussion in Section 2.1 as well as the previous discussion in this section, the strut angle of the small supporting element at the inflated state is larger for the OCS than that for the BVS. In contrast, the elastic recoiling force is smaller for the OCS than that for the BVS. As a result, the UHSR has a greater capacity to resist the elastic contraction, and the radial recoil of the OCS is lower than that of the BVS. Figure 13 illustrates the von Mises total mechanical strain of both the OCS and BVS at the inflated state. From Figure 13, it is observed that the strain of small supporting element of the OCS at the corner is larger than that of the BVS. θ_1 and θ_2 are calculated as approximately 96° and 81°, respectively, which proves the correctness of the aforementioned statements.

3.4.2. Axial Foreshortening. Axial foreshortening refers to the percentage change in the length of a stent between the crimping state and deflated state, which is usually expressed as

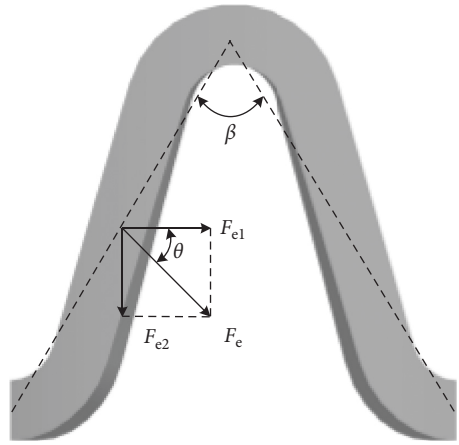

Figure 12: Diagram of supporting element under elastic recoiling force.

$$\text{axial foreshortening} = \left(1 - \frac{L_{\text{deflated}}}{L_{\text{crimp}}}\right) \times 100\%. \quad (14)$$

According to the analysis of the stent expansion, the axial foreshortening of the OCS was calculated as −3.0%, which indicates that the OCS is slightly elongated instead of being shortened during the expansion. For the BVS, the axial foreshortening was calculated as 1.4%, meaning that the OCS was shortened. Based on the discussion in Section 2.2, during inflation, the pressure exerted by the balloon is applied to the internal surface of the stent, causing supporting element to be subjected to the circumferential tension force. Under the action of circumferential tension force, supporting elements of both the OCS and BVS are gradually "straightened," resulting in a decrease of the supporting ring height. For the OCS, the curved structure is used to design the bridges, namely, c-shaped bridges, and the connecting positions of the bridges are set in the middle of the straight section of the supporting elements, which leads to the bending moments M_t caused by circumferential tension force F_{t1} and F_{t2} applied to both ends of the bridges, as shown in Figure 14. As a result, there is an elongation of the bridges along the axial direction, which compensates the shortening behavior of the supporting ring during expansion. In contrast, for the BVS, the straight rod-shaped bridges are used, which cannot be elongated during expansion. Therefore, the OCS is slightly elongated, whereas the BVS is shortened after expansion, and the results are shown in Figure 15, which illustrates the axial displacement of these two stents at original and inflated states.

3.4.3. Radial Force. Radial force refers to the capacity of a stent to withstand compressive loads [32], which can be characterized by compressive load-displacement curve during the compression process. To evaluate the radial force of the stents with various lengths, compressive load must be normalized by length as follows:

$$\text{normalized compressive load} = \frac{F}{L_{\text{deflated}}}, \quad (15)$$

where F is the compressive load and L_{deflated} is the length of the stent at the deflated state.

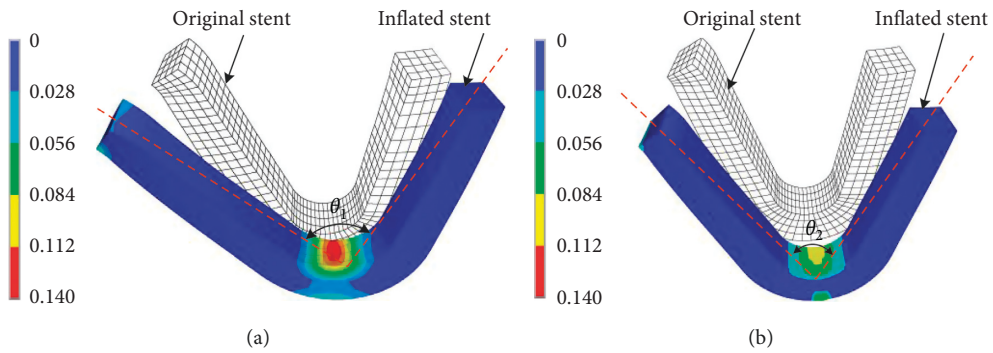

Figure 13: Local deformations of the stents at the inflated state: the supporting element of (a) the OCS and (b) the BVS.

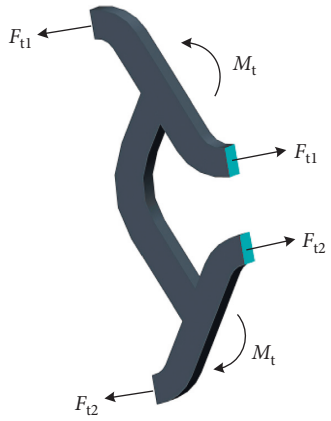

Figure 14: Diagram of force analysis of the c-shaped bridge during inflation.

The normalized compressive load (NCL)-displacement curves of the OCS and BVS were obtained based on planar compression simulation as shown in Figure 16. The contour plots in Figure 16 show the compressive displacement of the OCS and BVS along the x-direction, respectively. The radial force is the NCL at which the compressive displacement reaches half the stent outer diameter at the deflated state. As a result, the radial forces of the OCS and BVS can be calculated as 100.5 mN/mm and 77.7 mN/mm, respectively, which indicates that the OCS exhibits better radial force than BVS does and the capacity of the OCS is increased by approximately 30% comparing with that of the BVS. This simulation results support the conclusion drawn in Section 2.1 that utilization of UHSRs can effectively improve the radial force of polymeric stents.

The FEA results clearly showed that the radial force, radial recoil, and axial foreshortening of the OCS are all superior to those of the BVS, which demonstrated the rationality of the OCS.

4. *In Vitro* Tests

In vitro experiment is the most straightforward method to measure the mechanical performance of a stent and has been used as the main approach to evaluate the safety and effectiveness of a designed stent. Unfortunately, most of the reports on the mechanical performance evaluation of BPSs are performed only based on FEA results. In this section, the OCS and BVS prototypes are fabricated first. After that, the mechanical properties of the stents including the radial force, radial recoil, and axial foreshortening are tested using *in vitro* expansion and planar compression experiments.

4.1. Stent Prototype Fabrication. Polylactic acid (Ingeo 4032D, NatureWorks LLC, USA) was selected as the building material. Firstly, polylactic acid minitubes with an outer diameter of 2.40 mm and a wall thickness of 0.14 mm were fabricated using an extruder (HPE-100H, Davis-Standard LLC, USA). After that, the polymeric tubes were laser machined using a laser engraving machine (Starfemoto, Coherent-ROFIN Co. Ltd., USA). The fabricated OCS and BVS prototypes had the wall thickness uniformity higher than 93%, the ovality less than 2.1%, and the error of the strut width lower than $\pm 5\,\mu$m, as shown in Figure 17.

4.2. In Vitro Expansion Test. To evaluate the radial recoil and axial foreshortening of the OCS and BVS, *in vitro* expansion experiments were conducted based on ASTM F2079-09 [33] and ASTM F2081-06 [34] using an expansion setup including a balloon catheter (Quantum-Maverick 2 Monorail 3.0 × 25 mm, Boston Scientific, USA) and a pressure pump (LP-P-30S, Lepu Medical Technology (Beijing) CO., LTD., China). The diameter and length of the stents were measured by using a tool microscope (VTM-3020F, Suzhou Aoka Optical Instrument CO., LTD., China) with an accuracy of ±0.001 mm. It is noteworthy that due to the lack of special crimper and considering that the mechanical properties of the OCS and BVS are compared based on the same test conditions, stent crimping process was neglected, i.e., the stents were expanded from the original outer diameter of 2.40 mm to 3.00 mm. The radial recoil and axial foreshortening data were achieved by measuring at least three specimens for each test. Average value and standard deviation of each test were calculated.

4.3. In Vitro Planar Compression Test. Planar compression experiments were carried out using an electric universal testing machine (Model HD-B609B-S, Dongguan Haida

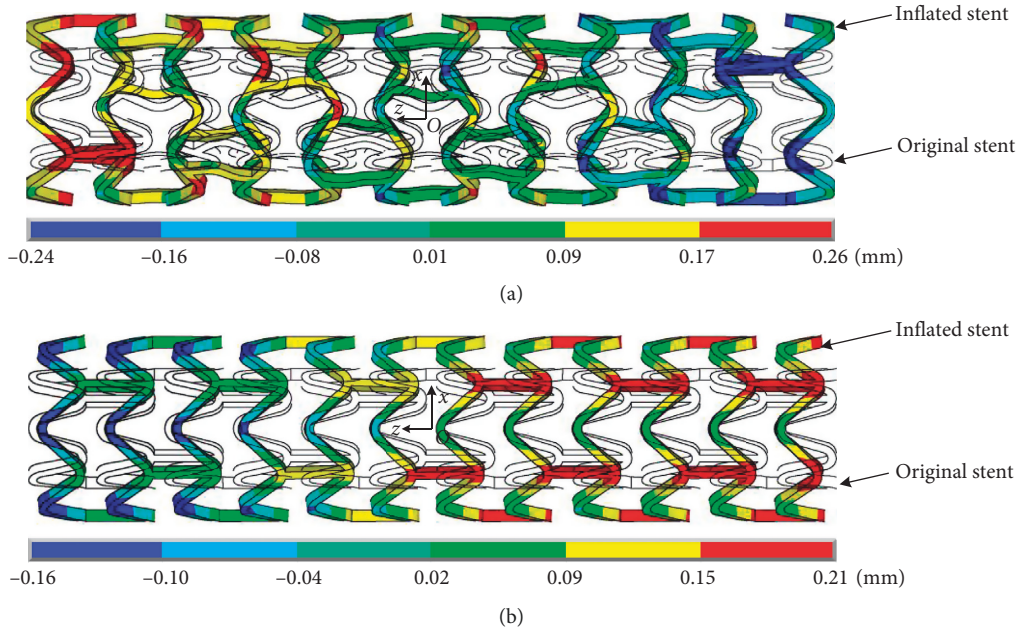

Figure 15: Deformations of the (a) OCS and (b) BVS at original and inflated states.

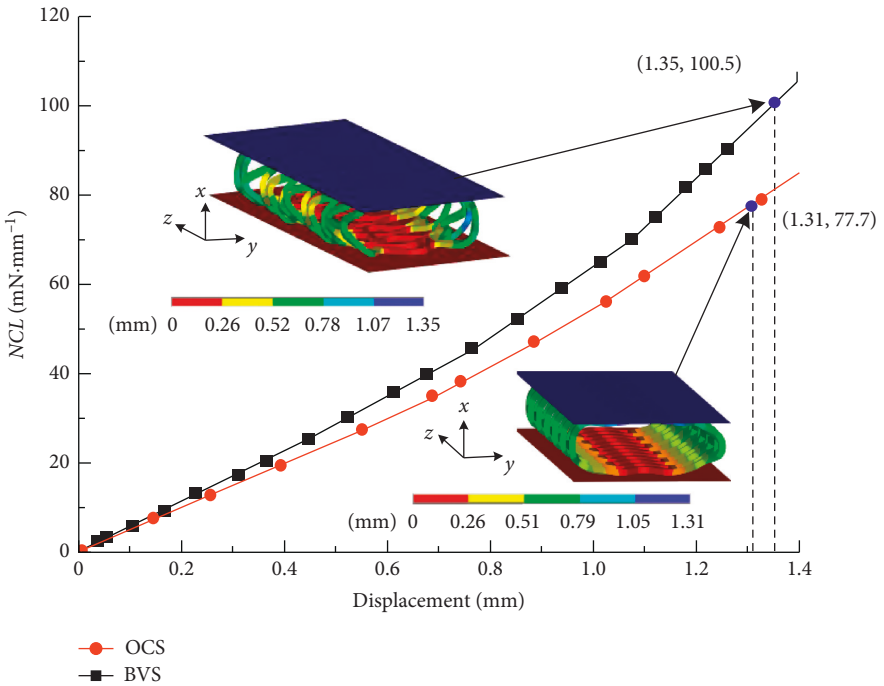

Figure 16: Normalized compressive load-displacement curves of the OCS and BVS during FEA.

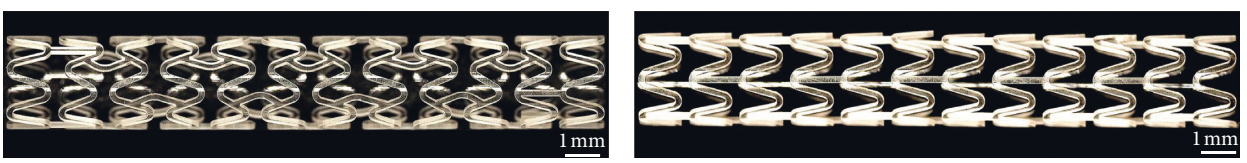

(a) (b)

Figure 17: The fabricated stent prototypes: (a) the OCS; (b) the BVS.

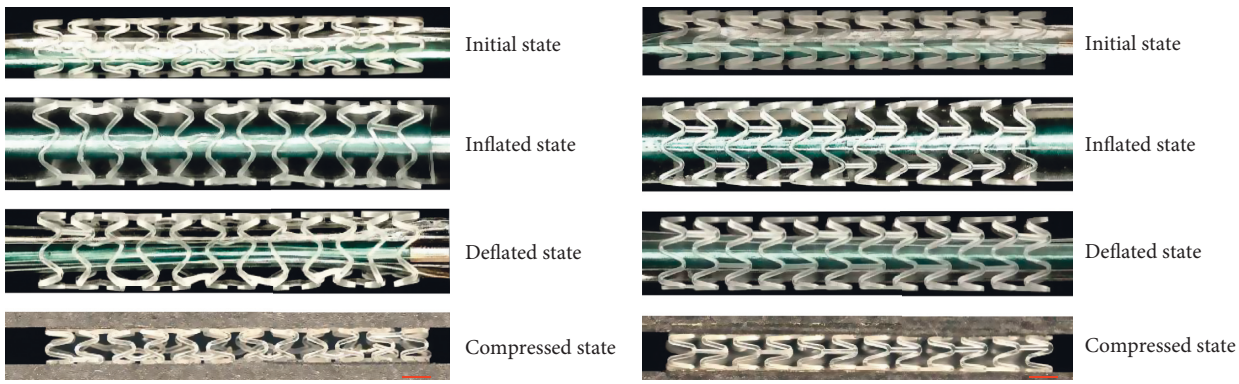

Figure 18: Deformations of the (a) OCS and (b) BVS at different states during *in vitro* expansion test and planar compression test. Scale bars: 1.0 mm.

Table 3: Outer diameters and lengths of OCS and BVS at different states during *in vitro* experiments.

Stent type	Original state		Inflated state		Deflated state	
	$D_{original}$ (mm)	$L_{original}$ (mm)	$D_{inflated}$ (mm)	$L_{inflated}$ (mm)	$D_{deflated}$ (mm)	$L_{deflated}$ (mm)
OCS	2.40 ± 0.01	15.50 ± 0.02	3.00 ± 0.02	16.08 ± 0.03	2.75 ± 0.02	15.83 ± 0.03
BVS	2.40 ± 0.01	16.10 ± 0.02	3.00 ± 0.02	15.57 ± 0.03	2.68 ± 0.02	15.86 ± 0.03

$D_{original}$: outer diameter of the original stent; $L_{original}$: length of the original stent.

Equipment Co., LTD., China) with a specially designed and lab-made planar compression clamps to measure the radial force of the OCS and BVS. The expanded stents were placed between the compression clamps and compressed at a rate of 0.3 mm/min. The force-displacement curves during compression were recorded. The radial force was the load at which the compressive displacement reaches half the outer diameter of the stents at the deflated state. Similar to the expansion test, the radial force data were obtained by measuring at least three specimens.

4.4. Experimental Results and Discussion. Deformations of the OCS and BVS at different states during *in vitro* expansion test and planar compression test are shown in Figure 18. During balloon inflation, the OCS and BVS expanded uniformly without circumferential rotation and strut fracture with the increase of balloon inner pressure, which was consistent with the finite element analysis results. After balloon deflation, the outer diameter of the stents decreased under the action of elastic recoiling force. During planar compression process, the stents were flattened with the increase of compressive load. The outer diameters and lengths of OCS and BVS at different states are shown in Table 3.

4.4.1. Radial Recoil and Axial Foreshortening. The radial recoil and axial foreshortening were obtained by using the *in vitro* stent expansion experiments, and the results are illustrated in Table 4. It should be noted that since the stent crimping was neglected in the experiments, the length of the crimped stent was replaced by the length of original stent when calculating the axial foreshortening.

Table 4: Radial recoil and axial foreshortening of the OCS and BVS.

Stent type	Radial recoil	Axial foreshortening
OCS	$8.3 \pm 0.4\%$	$-2.1 \pm 0.2\%$
BVS	$10.6 \pm 0.5\%$	$1.5 \pm 0.3\%$

From Table 4, it is found that the OCS exhibits much lower radial recoil comparing with that of BVS, and the reduction rate is approximately 22.0%. This conclusion is consistent with that obtained by FEA, while the simulated result is higher than the experimental result with the error less than 17.0%. This difference can be attributed to three possible reasons: (1) stent crimping was neglected in the experiments; (2) the radial displacement load was used to inflate the balloon in the simulation to reduce the requirement for high computational speed, whereas during the *in vitro* expansion test, the balloon was expanded by pressure load; and (3) deviations of wall thickness and ovality of the fabricated stent prototypes may affect the measurements, while the structural deviation effects are ignored during the simulation.

The axial foreshortenings of the OCS and BVS are $-2.1 \pm 0.2\%$ and $1.5 \pm 0.3\%$, respectively, which indicates that the OCS was elongated and the BVS was shortened during expansion. The results are also in accordance with the simulation results. However, due to the different formulas for calculating axial foreshortening in FEA and experiment, the difference between finite element results and experimental results was slightly larger.

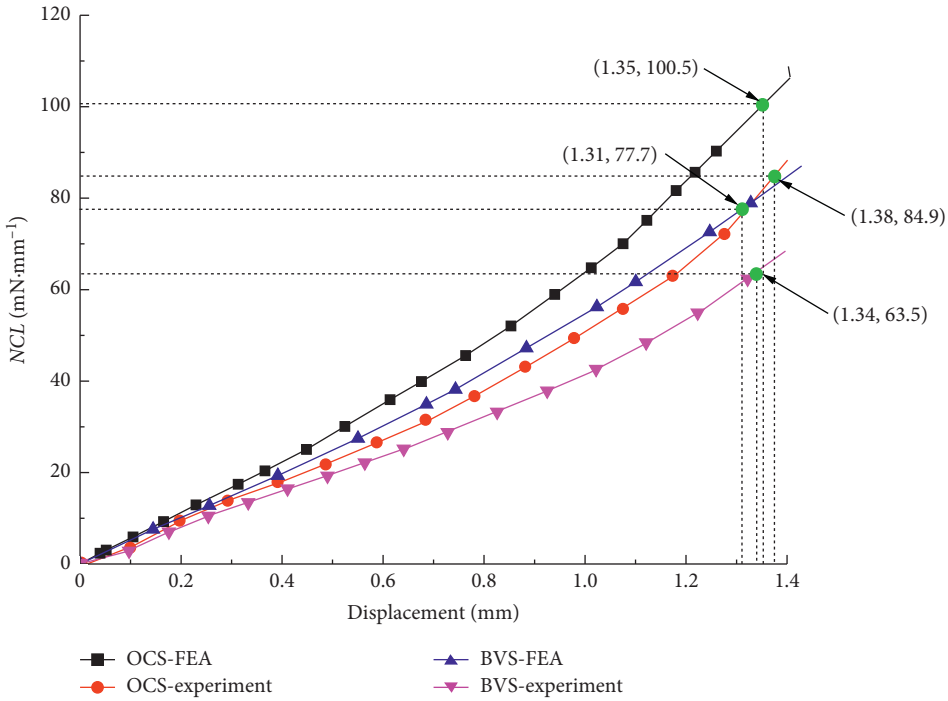

Figure 19: Normalized compressive load-displacement curves of the OCS and BVS during *in vitro* experiments and FEA.

4.4.2. Radial Force. Based on the planar compression experiments, the force-displacement curves of the OCS and BVS were obtained as shown in Figure 19. The radial force of the OCS and BVS are calculated as 84.9 ± 0.8 and 63.5 ± 0.6 mN/mm, respectively, indicating that the radial force of the OCS is approximately 34.0% greater than that of the BVS. The conclusion is consistent with the simulation result, while the FEA simulations appear to be slightly higher than the experimental measurements with the error less than 18.0%. The reasons for this difference mainly include two aspects: (1) stent crimping was neglected in the experiments (2) during the *in vitro* experiments, the nonuniform outer surface of the stents after expansion may lead to the invalid displacement before the stents and compressive plates completely contacting with each other at the initial compression state, which can decrease the radial force.

From the *in vitro* experimental results, it is concluded that all the mechanical properties including the radial force, radial recoil, and axial foreshortening of the OCS are better than those of the BVS, which further validates the rationality of the proposed OCS and the effectiveness of the finite element method to evaluate the mechanical properties.

5. Conclusions

In this study, a novel BPS with favorable radial force, radial recoil, and axial foreshortening has been proposed and investigated based on the force analysis of the supporting rings and bridges during stent implantation. A comparative analysis on the mechanical properties of the OCS and BVS has been conducted using both the finite element method and the *in vitro* experiments. Some key conclusions are summarized as follows:

(1) The mechanical properties of the OCS designed according to the proposed design method of BPS are considerably improved. Comparing with the commercial BVS, the proposed OCS exhibits a 30% increase in radial force, a 24% decrease in radial recoil, and the OCS is not shortened during expansion.

(2) Supporting ring is the main structural component affecting the radial force and radial recoil of stents. The utilization of the proposed UHSRs can contribute to improve these two mechanical properties.

(3) Axial foreshortening is mainly determined by the bridge structure as well as the connecting position of the bridge with the adjacent supporting rings. It can be improved by using bridges with a curved structure and setting the connecting position in the middle of the straight section of the supporting elements.

(4) The rationality of the proposed OCS and the effectiveness of the finite element method were verified by *in vitro* experiments. The design method combined with experimental verification can serve as a useful tool for designing BPS.

Data Availability

The data used to support the findings of this study are included within the article.

Conflicts of Interest

The authors declare that there are no conflicts of interest regarding the publication of this paper.

Acknowledgments

This study was funded by the National Natural Science Foundation of China (51675079 and 11502044), National Key R&D Program of China (2018YFA0703000), and the Fundamental Research Funds for the Central Universities (DUT17RC(3)104 and DUT19ZD202).

References

[1] P. McKavanagh, G. Zawadowski, N. Ahmed, and M. Kutryk, "The evolution of coronary stents," *Expert Review of Cardiovascular Therapy*, vol. 16, no. 3, pp. 219–228, 2018.

[2] H. Tan and R. Ananthakrishna, "A review of bioresorbable scaffolds: hype or hope?," *Singapore Medical Journal*, vol. 58, no. 9, pp. 512–515, 2017.

[3] J.-M. Ahn, D.-W. Park, S. J. Hong et al., "Bioresorbable vascular scaffold Korean expert panel report," *Korean Circulation Journal*, vol. 47, no. 6, pp. 795–810, 2017.

[4] S. Borhani, S. Hassanajili, S. H. Ahmadi Tafti, and S. Rabbani, "Cardiovascular stents: overview, evolution, and next generation," *Progress in Biomaterials*, vol. 7, no. 3, pp. 175–205, 2018.

[5] G. Caiazzo, I. D. Kilic, E. Fabris et al., "Absorb bioresorbable vascular scaffold: what have we learned after 5 years of clinical experience?," *International Journal of Cardiology*, vol. 201, pp. 129–136, 2015.

[6] J. S. Soares Jr. and J. E. Moore, "Biomechanical challenges to polymeric biodegradable stents," *Annals of Biomedical Engineering*, vol. 44, no. 2, pp. 560–579, 2016.

[7] T. Hu, C. Yang, S. Lin, Q. Yu, and G. Wang, "Biodegradable stents for coronary artery disease treatment: recent advances and future perspectives," *Materials Science and Engineering: C*, vol. 91, pp. 163–178, 2018.

[8] G. Niels, M. B. Carsten, S. Christine et al., "A biodegradable slotted tube stent based on poly(L-lactide) and poly(4-hydroxybutyrate) for rapid balloon-expansion," *Annals of Biomedical Engineering*, vol. 35, no. 12, pp. 2031–2038, 2007.

[9] S. H. Im, Y. Jung, and S. H. Kim, "Current status and future direction of biodegradable metallic and polymeric vascular scaffolds for next-generation stents," *Acta Biomaterialia*, vol. 60, pp. 3–22, 2017.

[10] J. P. Hytönen, J. Taavitsainen, S. Tarvainen, and S. Ylä-Herttuala, "Biodegradable coronary scaffolds: their future and clinical and technological challenges," *Cardiovascular Research*, vol. 114, no. 8, pp. 1063–1072, 2018.

[11] T. R. Welch, A. W. Nugent, and S. R. Veeram Reddy, "Biodegradable stents for congenital heart disease," *Interventional Cardiology Clinics*, vol. 8, no. 1, pp. 81–94, 2019.

[12] D. Lindholm and S. James, "Bioresorbable stents in PCI," *Current Cardiology Reports*, vol. 18, no. 8, pp. 1–6, 2016.

[13] V. Kočka, P. Toušek, and P. Widimský, "Absorb bioresorbable stents for the treatment of coronary artery disease," *Expert Review of Medical Devices*, vol. 12, no. 5, pp. 545–557, 2015.

[14] R. D. Alexy and D. S. Levi, "Materials and manufacturing technologies available for production of a pediatric bioabsorbable stent," *BioMed Research International*, vol. 2013, Article ID 137985, 11 pages, 2013.

[15] H. Y. Ang, Y. Y. Huang, S. T. Lim, P. Wong, M. Joner, and N. Foin, "Mechanical behavior of polymer-based vs. metallic-based bioresorbable stents," *Journal of Thoracic Disease*, vol. 9, no. 9, pp. S923–S934, 2017.

[16] M.-Y. Ho, C.-C. Chen, C.-Y. Wang et al., "The development of coronary artery stents: from bare-metal to bio-resorbable types," *Metals*, vol. 6, no. 7, p. 168, 2016.

[17] A. Schiavone, L. G. Zhao, and A. A. Abdel-Wahab, "Effects of material, coating, design and plaque composition on stent deployment inside a stenotic artery-finite element simulation," *Materials Science and Engineering: C*, vol. 42, pp. 479–488, 2014.

[18] W. Wu, L. Petrini, D. Gastaldi et al., "Finite element shape optimization for biodegradable magnesium alloy stents," *Annals of Biomedical Engineering*, vol. 38, no. 9, pp. 2829–2840, 2010.

[19] H.-M. Hsiao, Y.-H. Chiu, K.-H. Lee, and C.-H. Lin, "Computational modeling of effects of intravascular stent design on key mechanical and hemodynamic behavior," *Computer-Aided Design*, vol. 44, no. 8, pp. 757–765, 2012.

[20] X. Shen, Y.-Q. Deng, S. Ji, Z.-M. Xie, and H.-F. Zhu, "Flexibility behavior of coronary stents: the role of linker investigated with numerical simulation," *Journal of Mechanics in Medicine and Biology*, vol. 17, no. 8, p. 1750112, 2018.

[21] A. C. Bobel, S. Petisco, J. R. Sarasua, W. Wang, and P. E. Mchugh, "Computational bench testing to evaluate the short-term mechanical performance of a polymeric stent," *Cardiovascular Engineering and Technology*, vol. 6, no. 4, pp. 519–532, 2015.

[22] I.-H. Bae, K.-S. Lim, J.-K. Park et al., "Mechanical behavior and in vivo properties of newly designed bare metal stent for enhanced flexibility," *Journal of Industrial and Engineering Chemistry*, vol. 21, pp. 1295–1300, 2015.

[23] Q. Feng, W. Jiang, K. Sun et al., "Mechanical properties and in vivo performance of a novel sliding-lock bioabsorbable poly-p-dioxanone stent," *Journal of Materials Science: Materials in Medicine*, vol. 22, no. 10, pp. 2319–2327, 2011.

[24] C. V. Bourantas, Y. Zhang, V. Farooq, H. M. Garcia-Garcia, Y. Onuma, and P. W. Serruys, "Bioresorbable scaffolds: current evidence and ongoing clinical trials," *Current Cardiology Reports*, vol. 14, no. 5, pp. 626–634, 2012.

[25] D. Brie, P. Penson, M.-C. Serban et al., "Bioresorbable scaffold—a magic bullet for the treatment of coronary artery disease?," *International Journal of Cardiology*, vol. 215, pp. 47–59, 2016.

[26] J. Yang and N. Huang, "Mechanical formula for the plastic limit pressure of stent during expansion," *Acta Mechanica Sinica*, vol. 25, no. 6, pp. 795–801, 2009.

[27] D. Zhao, H. Wang, D. Wang, M. Wang, and D. Yao, "Experimental and numerical study of microchannel formation in rubber-assisted hot embossing with an open-channel mold," *Microsystem Technologies*, vol. 23, no. 5, pp. 1221–1227, 2017.

[28] H. Li, T. Liu, M. Wang et al., "Design optimization of stent and its dilatation balloon using kriging surrogate model," *BioMedical Engineering OnLine*, vol. 16, no. 1, p. 13, 2017.

[29] K. Takashima, T. Kitou, K. Mori, and K. Ikeuchi, "Simulation and experimental observation of contact conditions between stents and artery models," *Medical Engineering & Physics*, vol. 29, no. 3, pp. 326–335, 2007.

[30] L. Junlei, Z. Feng, Q. Xun, W. Peng, T. Lili, and Y. Ke, "Finite element analyses for optimization design of biodegradable magnesium alloy stent," *Materials Science and Engineering: C*, vol. 42, pp. 705–714, 2014.

[31] T. Y. Qiu, M. Song, and L. G. Zhao, "A computational study of crimping and expansion of bioresorbable polymeric stents," *Mechanics of Time-dependent Materials*, vol. 22, no. 2, pp. 273–290, 2018.

[32] R. G. Pauck and B. D. Reddy, "Computational analysis of the radial mechanical performance of PLLA coronary artery stents," *Medical Engineering & Physics*, vol. 37, no. 1, pp. 7–12, 2015.

[33] ASTM International. F2079-09, *Standard Test Method for Measuring Intrinsic Elastic Recoil of Balloon-Expandable Stents*, ASTM International, West Conshohocken, PA, USA, 2017.

[34] ASTM International. F2081-06, *Standard Guide for Characterization and Presentation of the Dimensional Attributes of Vascular Stents*, ASTM International, West Conshohocken, PA, USA, 2017.